J. Fluid Mech. (2007), *vol.* 572, *pp.* 339–366.
doi:10.1017/S0022112006003727 Printed in the United Kingdom

Effects of homogeneous condensation in compressible flows: Ludwieg-tube experiments and simulations

By XISHENG LUO[1]†, GRAZIA LAMANNA[2], A. P. C. HOLTEN[1] AND M. E. H. van DONGEN[1]

[1]Department of Applied Physics, Eindhoven University of Technology, Eindhoven, The Netherlands

[2]Institute of Aerospace Thermodynamics, Universität Stuttgart, Stuttgart, Germany

(Received 27 December 2005 and in revised form 14 July 2006)

Effects of homogeneous nucleation and subsequent droplet growth in compressible flows in humid nitrogen are investigated numerically and experimentally. A Ludwieg tube is employed to produce expansion flows. Corresponding to different configurations, three types of experiment are carried out in such a tube. First, the phase transition in a strong unsteady expansion wave is investigated to demonstrate the mutual interaction between the unsteady flow and the condensation process and also the formation of condensation-induced shock waves. The role of condensation-induced shocks in the gradual transition from a frozen initial structure to an equilibrium structure is explained. Second, the condensing flow in a slender supersonic nozzle G2 is considered. Particular attention is given to condensation-induced oscillations and to the transition from symmetrical mode-1 oscillations to asymmetrical mode-2 oscillations in a starting nozzle flow, as first observed by Adam & Schnerr. The transition is also found numerically, but the amplitude, frequency and transition time are not yet well predicted. Third, a sharp-edged obstacle is placed in the tube to generate a starting vortex. Condensation in the vortex is found. Owing to the release of latent heat of condensation, an increase in the pressure and temperature in the vortex core is observed. Condensation-induced shock waves are found, for a sufficiently high initial saturation ratio, which interact with the starting vortex, resulting in a very complex flow. As time proceeds, a subsonic or transonic free jet is formed downstream of the sharp-edged obstacle, which becomes oscillatory for a relatively high main-flow velocity and for a sufficiently high humidity.

1. Introduction

The nucleation of vapour to liquid is the process of formation of the smallest stable droplets possible, so-called critical clusters. If the process takes place in the absence of foreign agents such as ions or dust particles, it is termed homogeneous nucleation (Abraham 1974; Kashchiev 2000). In most cases, the homogeneous nucleation rate strongly depends on the degree of supersaturation S, defined here as the ratio of the actual vapour pressure p_v and the saturated vapour pressure p_{vs}, i.e. $S = p_v/p_{vs}$. If the supersaturation is high enough, clusters that are large enough to act as condensation

† Present address: Shock Wave Laboratory, RWTH-Aachen, 52056, Aachen, Germany. xLuo@swl.rwth-aachen.de.

nuclei are formed spontaneously in the gas phase, i.e. homogeneous nucleation takes place. Once a stable cluster has been formed, it will grow until phase equilibrium is achieved. Condensation phenomena are often found in nature and in industry, such as in steam turbines, in supersonic wind tunnels, in vortices around wing tips or above the suction side of wings in transonic flight, in phase-separation devices and in high-pressure pipelines after the sudden opening of pressure-relief valves. It should be mentioned that also heterogeneous nuclei may play an important role. The relative importance of homogeneous and heterogeneous nucleation depends on the maximum value of the supersaturation, and therefore on the cooling rate, and also on the concentration and properties of the heterogeneous nuclei present. Here we restrict ourselves to homogeneous processes.

Apart from its technological relevance, nucleation and condensation phenomena in compressible flows are also important from a more fundamental point of view. Nucleation rates are strongly dependent on supersaturation. Diffusion cloud chambers (Wegener & Mirabel 1987) cover the range of low supersaturation and correspondingly 'low' nucleation rates. For the intermediate range of supersaturation, use is made of expansion cloud chambers (Wölk & Strey 2001) and of expansion-wave tubes (Holten, Labetski & van Dongen 2005). Recently, Laval nozzles have been used as sources of information about nucleation rates in the highest supersaturation regime, in which critical clusters consist of not more than a few molecules (Heath *et al.* 2003). For a further development of these experimental facilities and for the exploration of new ideas, the relation between gas dynamics and cloud physics needs to be well understood.

Gas-dynamic studies of nucleation and condensation have a history of about 70 years. It all started with the observation of peculiar and unexpected disturbances just downstream of the throat of a supersonic wind tunnel, visualized by Busemann in Göttingen and presented by Prandtl at the Volta Conference in Rome in 1935 (Prandtl 1936). It was proposed by Wieselsberger somewhat later that the disturbances were shock waves somehow caused by the condensation of water vapour in the transonic flow near the nozzle throat. In the decades that followed, the phenomenon was extensively investigated, in humid carrier gases as well as in steam, experimentally as well as theoretically. It became clear that owing to the fast isentropic expansion of the gas and/or vapour particles that are passing the nozzle, the vapour may attain a high value of supersaturation. Subsequently, a relatively large number of critical droplets is formed, owing to homogeneous nucleation. The growing droplets lead to the release of latent heat, to be absorbed by the flowing gas and/or vapour. This makes nozzle flows with condensation examples of diabatic gas dynamics. If the release of heat occurs in the supersonic part of the nozzle, a positive pressure disturbance is to be expected, in agreement with observations. For increasing humidity, if the geometry and other initial conditions are kept fixed, the pressure disturbance evolves into a shock wave, positioned just upstream of the locus of heat release and having a subtle interplay with all the physical processes involved. If the humidity is even further increased, and the geometry is such that the condensation occurs just downstream of the nozzle throat, it is possible that steady-state solutions no longer exist and that the flow becomes oscillatory. Such self-sustained oscillations are directly related to the limited capacity of a steady compressible flow to absorb heat, even vanishing completely at Mach number unity. A new, essentially two-dimensional, mode of oscillation was been reported by Adam & Schnerr (1997). Lamanna (2000) and Lamanna, van Poppel & van Dongen (2002) combined interferometric studies of unsteady condensing flows in a Laval nozzle with measurements of droplet size. Condensation-induced disturbances,

shock waves and condensation-induced instabilities have also been found in supersonic expansion flows around a sharp corner, so-called Prandtl–Meyer corner expansions.

A supersaturated state of a vapour, either pure or diluted in a carrier gas, can also be obtained in an unsteady expansion of the vapour and/or gas, such as can be realized in a shock tube. Condensation occurs, with release of latent heat, which leads to a pressure and temperature increase and again to the formation of a weak shock wave embedded in the strong nonlinear expansion wave. Systematic studies have been performed on the dependence on the onset conditions, i.e. the conditions at which the droplet cloud can be first detected, the initial humidity and the water-mass fraction, for different carrier gases.

Very useful and extensive summaries of condensing compressible flows have been given by, among others, Wegener & Mack (1958), Wegener (1969, 1975), Wegener & Wu (1977), Kotake & Glass (1978) and Zierep (1990); these works include interesting historical notes.

Most numerical and theoretical studies of gas-dynamic flows with condensation are based on the concepts formulated first by Oswatitsch (1942). He combined the classical nucleation theory with the Hertz–Knudsen model for droplet growth and the equations of diabatic gas dynamics. Numerical solutions for Laval nozzle flows with condensation-induced oscillations were presented by first Saltanov & Tkalenko (1975) for a quasi-one-dimensional configuration and by White & Young (1993) for the unsteady two-dimensional case. A new numerical approach was introduced by Schnerr & Dohrmann (1990) and Mundinger (1994), who described the nucleation and condensation process by solving the conservation laws for the first four moments of the droplet-size distribution function, as proposed by Hill (1966). This numerical approach was successfully applied by Schnerr, Adam & Mundinger (1994) to condensing flows in circular-arc nozzles. Put *et al.* (2001) and Put (2003) described a generally applicable numerical method to simulate steady three-dimensional flows of condensing real gases.

Extensive theoretical studies of condensing flows in Laval nozzles, corner expansions and unsteady expansion waves have been performed by Delale, Schnerr & Zierep (1993*a*,*b*,*c*), Delale & van Dongen (1998) and Delale, Lamanna & van Dongen (2001). Their theory is based on the application of asymptotic analytical methods, first applied to condensation gas dynamics by Blythe & Shih (1976).

Condensation phenomena in transonic flow around airfoils were studied, experimentally and numerically, by Schnerr & Dohrmann (1990, 1994). Studies based on a transonic small-disturbance theory were reported by Rusak & Lee (2000) and Lee & Rusak (2001*a*,*b*). The work presented here has been inspired by the parallel development of a gas-dynamic facility for nucleation research, the pulse-expansion wave tube (Looijmans & van Dongen 1997). Many exciting new results on nucleation and droplet growth have been obtained for a variety of gas–vapour mixtures (Luijten, Peeters & van Dongen 1999; Peeters, Pieterse & van Dongen 2004; Holten, Labetski & van Dongen 2005). In the same period a new, efficient, numerical method has been developed. The details of the method and its application to the pulse-expansion wave tube are described in Luo *et al.* (2006). A brief summary will be given in § 3.

The objective of this research is to investigate some typical condensation-induced phenomena, as observed in a Ludwieg tube. Three different experiments are considered. The first two have been studied before: condensation-induced shock-wave formation in an unsteady expansion fan and condensation-induced oscillations in a slender Laval nozzle. While some new aspects will be discussed, these experiments also serve as an introduction to the third experiment: the interaction of an unsteady

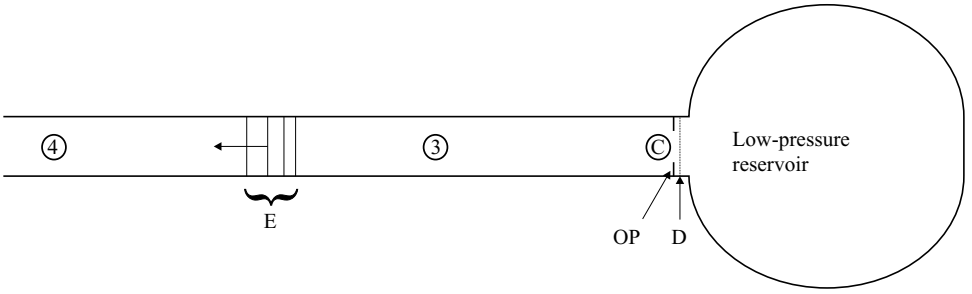

FIGURE 1. Ludwieg tube connected to a low-pressure reservoir. OP, orifice plate; D, diaphragm. Regions: 4, rest; 3, steady flow to the right; c, choked flow at orifice.

expansion fan in humid nitrogen with a sharp-edged obstacle, which leads to a starting vortex and ultimately to the development of a free jet. We shall investigate the effects of nucleation and condensation on these unsteady two-dimensional flow fields.

This paper is organized as follows. In § 2 the experimental setup and methods are briefly described. Section 3 is dedicated to a concise discussion of the condensation model and its implementation in a numerical method. Phase transitions in unsteady rarefaction waves are studied in § 4. In § 5, the experimental and numerical results for the supersonic nozzle G2 will be compared. Section 6 focuses on the problem of vortex shedding from a sharp-edged obstacle in the Ludwieg tube. The effects of condensation on the starting vortex and on the free jets will be investigated experimentally and numerically. Conclusions are drawn in § 7.

2. Experimental setup and methods

In this section, we will introduce the experimental setup including the Ludwieg tube, the supersonic nozzle G2 and the sharp-edged obstacle. The density field is recorded by means of holographic interferometry, which will be briefly discussed too. A detailed description of the experimental method of double-exposure holographic interferometry can be found in Lamanna (2000).

2.1. *Ludwieg tube and its configurations*

This gas-dynamic facility, now known as the Ludwieg tube, was first introduced by H. Ludwieg (1955, 1957). The tube was initially developed for the testing of vehicles flying at high transonic speeds. Its application to condensing nozzle flows was first proposed and successfully applied by Wegener & Wu (1977). The TUE Ludwieg tube has a square cross section of $10 \times 10\,\mathrm{cm}^2$ and length 12.0 m. According to different experimental purposes, the tube has been used in three configurations.

2.1.1. *Ludwieg tube: basic configuration*

In the basic configuration, depicted schematically in figure 1, an orifice is used to locally decrease the cross-sectional area A to A_T, and a diaphragm initially separates the tube from a low-pressure reservoir. First, the tube is filled with the test gas and the low-pressure reservoir is evacuated. Then, by breaking the diaphragm, an expansion wave is generated which travels into the tube, resulting in a flow from the tube (at high pressure) to the reservoir (at low pressure). The orifice in the tube acts as a throat that chokes the flow, i.e. the Mach number at the orifice equals unity ($M_c = 1$). Upon the passage of the expansion wave, a steady flow is established in region 3 with a Mach number that follows directly from the area ratio of the tube and the

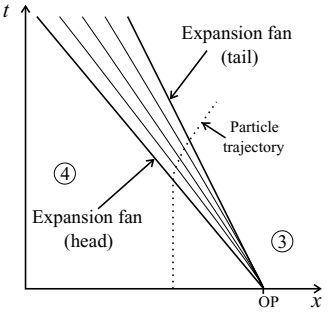

FIGURE 2. (x, t)-diagram of waves in the expansion tube. OP is the orifice plate.

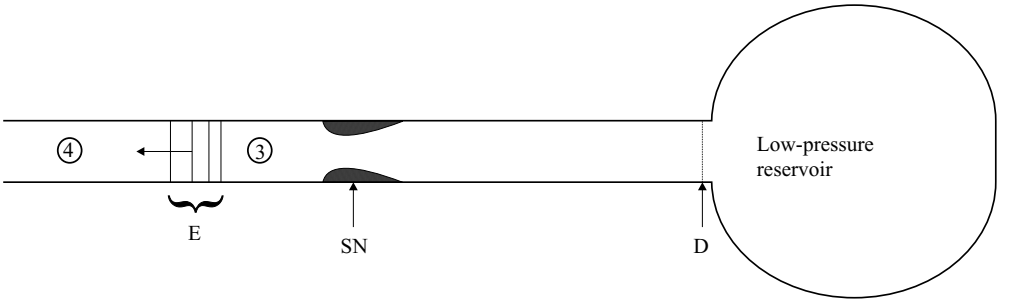

FIGURE 3. Ludwieg tube with a supersonic nozzle; the flow chokes at the throat of the nozzle and becomes supersonic downstream from the throat. SN, supersonic nozzle; D, diaphragm; E, expansion fan. Regions: 4, rest; 3, steady flow to the right.

orifice, A/A_T. For a calorically perfect gas, with specific heat ratio γ, this relation is (Owczarek 1964):

$$\frac{A}{A_T} = \frac{1}{M_3}\left[\frac{2}{\gamma+1}\left(1+\frac{\gamma-1}{2}M_3^2\right)\right]^{(\gamma+1)/(2(\gamma-1))}. \tag{2.1}$$

An (x, t)-diagram of the relevant wave pattern and a typical path of a gas 'particle' are shown in figure 2.

In our experiments, nitrogen ($\gamma = 1.4$) was used in the tube under atmospheric pressure at a temperature close to 20 °C. The orifice plate was located at 2.0 cm upstream of the diaphragm.

2.1.2. *Ludwieg tube: Laval nozzle*

For the case of condensing supersonic nozzle flow, the second configuration, as shown in figure 3, is used. In this configuration, the choking place is at the throat of the nozzle since the orifice plate is not used. The flow downstream from the throat becomes supersonic and, since the temperature of the flow decreases further in the divergent part of the nozzle, condensation takes place. Depending on the conditions and geometry, a shock wave is formed owing to the condensation process, and condensation-induced oscillations may be generated.

In the study reported in the present paper, a slender two-dimensional nozzle (G2) was placed at a distance of 1.0 m from the diaphragm at a windowed position along the tube. Its exit isentropic Mach number was $M = 2.0$. Owing to its low cooling rate, the nozzle can produce optically detectable droplets with measurable droplet

Nozzle	Type	Length (cm)	h^* (cm)	R^*_{0-} (cm)	R^*_{0+} (cm)	$(-\mathrm{d}T/\mathrm{d}x)^*$ ($\mathrm{K\,cm^{-1}}$)	$(-\mathrm{d}T/\mathrm{d}t)^*$ ($\mathrm{K\,\mu s^{-1}}$)
G2	parallel outflow	50	2	30	400	3.15	0.100

TABLE 1. Geometric characteristics, temperature gradients and cooling rates for nozzle G2. The temperature gradient and the cooling rate are evaluated using the curvature downstream from the nozzle throat at the representative stagnation temperature, $T_0 = 293\,\mathrm{K}$.

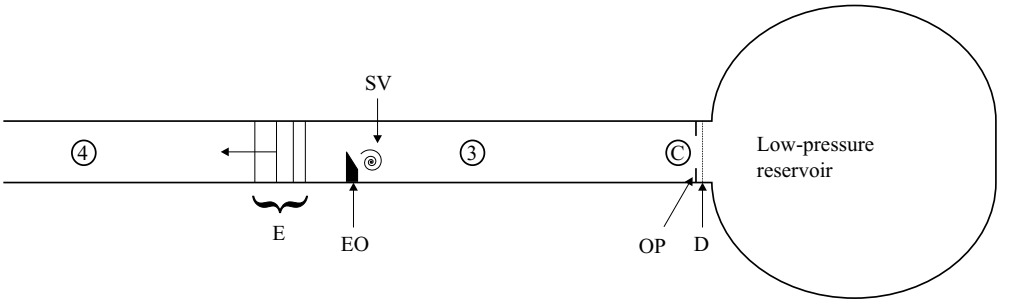

FIGURE 4. Ludwieg tube with a sharp-edged obstacle. OP, orifice plate; D, diaphragm; EO, sharp-edged obstacle; SV, starting vortex. Regions: 4, rest; 3, steady flow to the right; c, choked flow at the orifice.

sizes. The nozzle specifications are given in table 1, in which the symbols R^*_{0-} and R^*_{0+} indicate the radii of curvature upstream and downstream of the nozzle throat, respectively; while h^* denotes the throat height.

2.1.3. *Ludwieg tube: sharp-edged obstacle*

To generate a starting vortex, a two-dimensional sharp-edged obstacle O was placed at 73.0 cm from the diaphragm; this forms the third configuration of the Ludwieg tube, as shown in figure 4. When the expansion wave passes the sharp-edged obstacle, flow separation occurs at the sharp edge and a starting vortex is created, which evolves in time. Because the temperature in the vortex is lower than that of the surrounding mixture, condensation is expected in this region.

The obstacle has a top angle of 30° and height 4.0 cm. A side view of the obstacle is shown in figure 5(*a*). To measure the pressure field, three Kulite transducers are employed. Figure 5(*b*) displays the positioning of the transducers in a wall plate. This plate can be rotated freely in such a way that the transducers can be used to measure the wall-pressure distribution along lines of arbitrary orientation with respect to the tube axis. When the plate is fixed in the position shown in figure 5(*b*), the transducer in the top position is at a distance of 7.0 mm from the centre of the window and the distance from the neighbouring transducers is 14.0 mm.

2.2. *Experimental setup*

A schematic diagram of the experimental setup is shown in figure 6 for the third configuration. The tube is connected to a vacuum tank which has a volume of $0.4\,\mathrm{m^3}$. A polyester diaphragm (Melinex polyester film) of 20 μm thickness separates the test section from the vacuum vessel. The diaphragm rests against cross-shaped supports with resistance wires mounted on them (Kanthal wires, $\phi = 0.1\,\mathrm{mm}$, $R = 150\,\Omega\mathrm{m^{-1}}$) and can be quickly broken by electrically heating the wires. A recirculation system is also connected to the tube, by valves V_1 and V_3. It consists of a circulation pump CP,

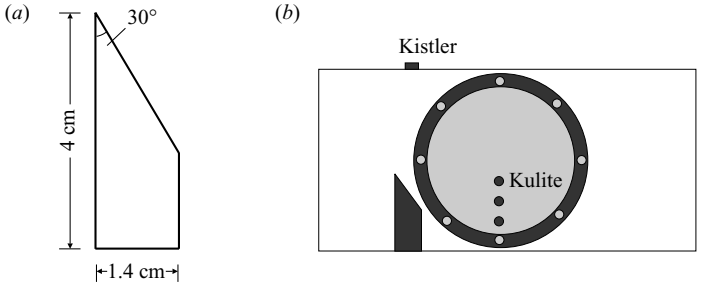

FIGURE 5. (*a*) Side view of the sharp-edged obstacle: top angle, 30°; height, 4.0 cm. (*b*) Test window with one Kistler and three Kulite pressure transducers.

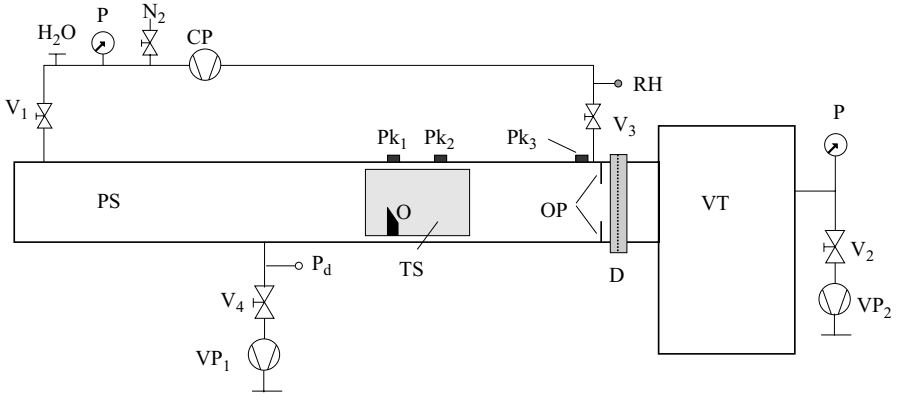

FIGURE 6. Schematic diagram of the Ludwieg-tube setup. PS, pressurized section; TS, test section; VT, vacuum tank; D, diaphragm; OP, orifice plate; CP, circulation pump; P, pressure gauge; RH, Humicap sensor; $Pk_{1,2,3}$, pressure transducers; $VP_{1,2}$, vacuum pumps; $V_{1,2,3,4}$, valves; P_d, Barocel (600A).

a water injector (H_2O) and a gas injector (N_2), a pressure gauge P and a Humicap sensor RH (Vaisala 234), which is used to measure the saturation ratio. Pressure measurements from Kistler transducers are performed in the tube at three different locations, $Pk_{1,2,3}$, as indicated in figure 6. The transducers $Pk_{1,2}$ are placed in the test section while the transducer Pk_3 is situated near the diaphragm (15 cm from the diaphragm) and is used to trigger the system.

All data from the Kistler transducers and from the Kulite transducers are recorded by a LeCroy transient recorder (Model 8013A, module 6810).

2.3. *Double-exposure holographic interferometry*

In the experiments the density field is recorded by means of holographic interferometry, a recording method that stores both the amplitude and phase of a wave. A holographic recording is made by simultaneously illuminating the holographic plate with the object wave and the reference wave. This results in an interference pattern, which is stored on the plate. After the recording, the plate is processed and the intensity pattern is converted to a transmission pattern. Then, to view the recorded image, the reconstruction of the hologram has to be carried out by re-illuminating the plate with the reference wave.

Figure 7 shows the optical configuration for performing holographic interferometry. The light source consists of two lasers, a continuous He–Ne laser ($\lambda = 632.8$ nm,

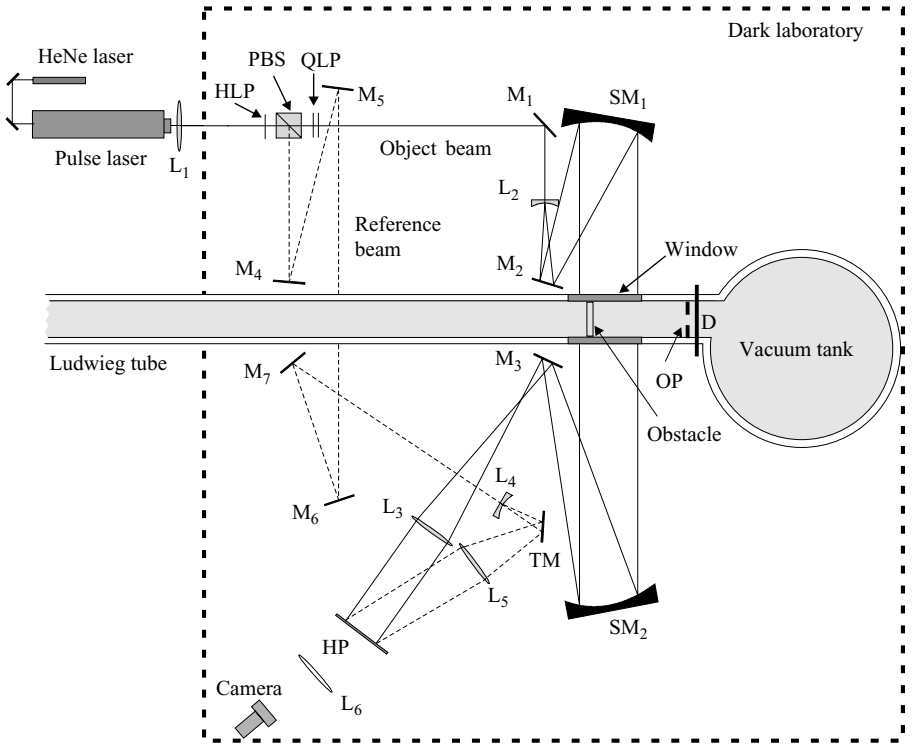

FIGURE 7. The optical configuration for holographic interferometry. $L_{1,3,5,6}$, convex lenses; $L_{2,4}$, concave lenses; TM, tilting mirror; $M_{1,\ldots,7}$, mirrors; $SM_{1,2}$, spherical mirrors; HLP, $\lambda/2$ plate; QLP, $\lambda/4$ plate; HP, holographic plate; D, diaphragm; OP, orifice plate.

20 mW) and a pulsed ruby laser (a 30 ns pulse at wavelength $\lambda = 694.3$ nm in an energy range of 0.01–1 J). The He–Ne laser is used to align the setup and the pulse laser is used to record the hologram.

2.4. *Preparation of the humid gas, initial state and total conditions*

Before starting a new experiment, a diaphragm has to be installed. Then both the tube connected to the recirculation circuit and the vacuum tank are evacuated, with the pumps VP1 and VP2, respectively (figure 6). Once the pressure in the tube is lower than 10 Pa, the evacuation process (including the recirculation part) is stopped and the circulation pump CP is turned on. Distilled water is then injected by the water injector (H_2O). The Humicap humidity signal is continuously monitored on a digital multimeter and on an oscilloscope display. The oscilloscope is set to a large time scale (20 s per division) in order to observe the humidity as a function of time. After the humidity has stabilized, dry nitrogen from the gas injector (N_2) is added slowly into the tube. Then the circulation pump is turned off, and the valves are all closed to prevent any unwanted influence. The stabilization of humidity normally takes several hours.

The initial saturation ratio is deduced from the humidity sensor and is denoted as S_{ini}. The initial temperature and pressure are p_0 and T_0. In the second configuration, the Laval-nozzle experiment, it is useful to define the 'total' or stagnation conditions upstream of the Laval nozzle, indicated by the subscript 'o'. The gas flow upstream of the Laval nozzle has experienced a slight isentropic expansion before it enters the Laval nozzle. Because of the passage of the transmitted expansion wave, the

temperature is isentropically related to the measured pressure, and the velocity u_3 follows from the equation of one-dimensional non-stationary gas dynamics (figure 3) (Courant & Friedrichs 1985),

$$u_3 = \frac{2}{\gamma - 1}(c_0 - c_3), \tag{2.2}$$

with sound speed $c = \sqrt{\gamma RT}$ and R the specific gas constant of the mixture. From u_3, the sound speed c_3, pressure p_3 temperature T_3, the total pressure and total temperature can be deduced according to their definitions (Owczarek 1964):

$$T_o = T_3\left(1 + \frac{\gamma - 1}{2}M_3^2\right), \qquad p_o = p_3\left(\frac{T_o}{T_3}\right)^{\gamma/(\gamma-1)}. \tag{2.3}$$

The 'total' saturation ratio S_o is related to S_{ini} according to

$$S_o = S_{ini}\frac{p_o}{p_0}\frac{p_{vs}(T_0)}{p_{vs}(T_o)}, \tag{2.4}$$

where $p_{vs}(T)$ is the saturation pressure and is expressed as (Vargaftik 1975)

$$p_{vs}(T) = 610.8\exp[-5.1421\ln(T/273.15) - 6828.77(1/T - 1/273.15)]. \tag{2.5}$$

In all cases $S_o \geqslant S_{ini}$. It is also possible that $S_o > 1$.

3. Condensation model and numerical method

Different condensation models, referring to specific combinations of nucleation theory, droplet-growth formulation and thermodynamic properties, have been developed and implemented in numerical methods. A simplifying assumption underlying all variants of classical nucleation theories is the 'capillarity approximation', which implies the use of macroscopic thermodynamic equilibrium properties to describe non-equilibrium microscopic clusters. In some cases even these macroscopic properties are not available. It is known, for example, that water vapour tends to nucleate to supercooled water even at a temperature below the so-called homogeneous ice-nucleation limit, 235 K, where no thermodynamic properties can be determined in quasi-steady-state experiments (Koop 2004). It should also be noted that empirical nucleation rates are only available in a limited range of temperatures and supersaturations. Recent overviews of experimental nucleation rates for water were given by Wölk *et al.* (2002) and Holten *et al.* (2005).

In our numerical study we applied a condensation model consisting of the reduced internally consistent classical nucleation theory (ICCT) nucleation model (Luijten 1998; Luijten *et al.* 1999) and the explicit droplet-growth formulation by Gyarmathy (Gyarmathy 1982; Peeters, Luijten & van Dongen 2001). The temperature difference between the droplets and the surrounding gas was taken into account by applying a wet-bulb approximation. The surface tension of water implemented in the numerical method was based on an extrapolation of empirical data (Lamanna 2000).

The fluid-dynamical behaviour of the two-phase system of gas and/or vapour and droplets is described by a system of conservation equations, supplemented by a description of the phase transition of the condensate mass. For the condensate mass the conservation of the liquid phase is described by a finite number of moments of the size distribution function (Hill 1966). The governing equation for the complete system can be considered as a combination of the moment equations of the size distribution and the Euler equations for time-dependent two-dimensional flow. On the basis of the

Diaphragm	Orifice	1	2	3	4
0	2.0	15.5	84.7	565.6	1207.4

TABLE 2. Positions in cm of the four Kistler pressure transducers in the Ludwieg tube in the basic configuration. Distances are measured from the position of the diaphragm.

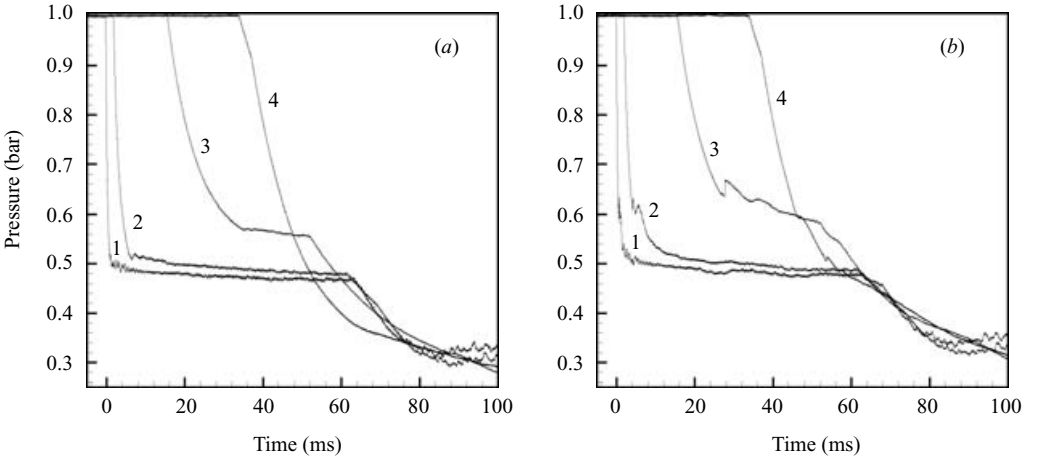

FIGURE 8. Experimental results of pressure histories from four locations in a Ludwieg tube: (*a*) dry, (*b*) wet. $S_{ini} = 0.805$.

fractional-step method (Oran & Boris 1987), the governing equations are split into two parts, a homogeneous part without source terms and an inhomogeneous part with the source terms due to the phase transition. The homogeneous part is solved by applying the same method as used in VAS2D, developed by Sun (1998) and Sun & Takayama (1999) for compressible flows. For the inhomogeneous part the treatment by Mundinger (1994) and Prast (1997) was followed. The combination of the two methods has been developed into a new numerical method: ASCE2D (two-dimensional and axisymmetric adaptive solver for condensation and evaporation) (Luo *et al.* 2006). In this method, the governing equations are discretized on an unstructured quadrilateral mesh that adapts to the time-dependent flow. The accuracy of this numerical method and the influence of mesh adaptation on the convergence of the numerical results were investigated by Luo (2004). On the basis of that study, the mesh size adopted for the numerical simulations of the three configurations is about $2 \times 2\,\mathrm{mm}^2$ with an adaptation level of 4. For a detailed description of the condensation model and the numerical method, the reader is referred to Luo (2004) and Luo *et al.* (2006).

4. Homogeneous condensation in unsteady rarefaction waves

An expansion wave travelling in a humid gas may cause a state of supersaturation, leading to nucleation and droplet growth. We investigated this wave-induced condensation in a Ludwieg tube by using the basic configuration. Four pressure transducers (Kistler) were mounted in the tube with their positions as listed in table 2.

The pressure histories of the dry and wet cases are shown in figure 8 for an orifice of $9 \times 9\,\mathrm{cm}^2$. After diaphragm rupture, the gas in the tube is accelerated and adiabatically expanded by the passing expansion wave towards a quasi-steady state

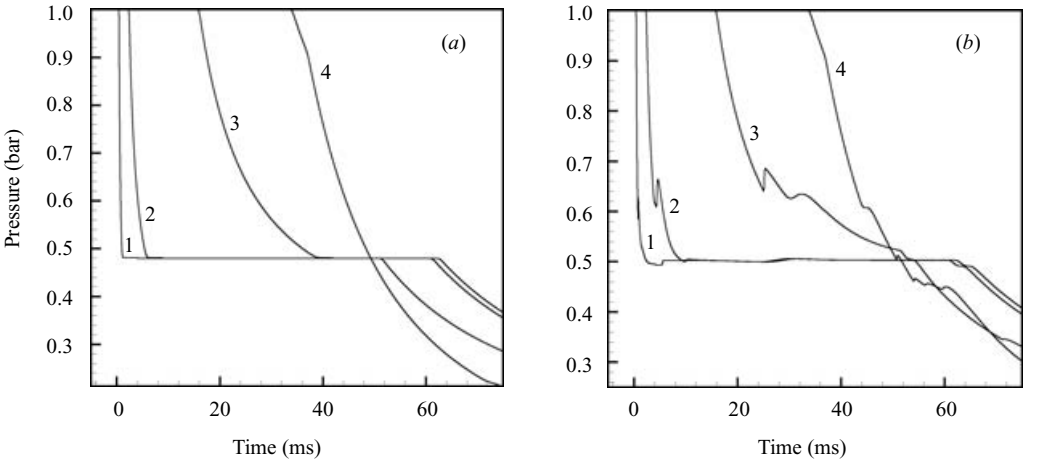

FIGURE 9. Numerical pressure histories from four locations in a Ludwieg tube: (*a*) dry, (*b*) wet. $S_{ini} = 0.805$.

with almost constant pressure and flow Mach number. This can clearly be observed as the plateau region, which is terminated by the arrival of the wave reflected from the end wall of the tube. Because the expansion is rather strong (the steady flow after the expansion wave has Mach number 0.25), wall friction and heat transfer affect the flow. This explains the increase in the plateau pressure with the distance from the diaphragm in the dry case; for instance the plateau pressure at position 3 is about 0.56 bar, which is higher than that at position 2 (0.5 bar). For the wet case, if the supersaturation is sufficiently high, droplets are generated and start to grow at an approximately constant temperature in the expansion wave front. In gas-dynamic terms this corresponds to a particular 'characteristic' (Courant & Friedrichs 1985) that propagates with the local speed of sound with respect to the local gas velocity, i.e. $u-c$ with u the local gas velocity and c the local speed of sound. The droplets formed will follow the gas particles. After some delay the increase in the liquid mass fraction will attain a maximum value. This also means that the production of latent heat attains a maximum there, i.e. approximately at the locus of the characteristic within the expansion wave front. Owing to the unsteady generation of heat, compression waves will be generated, both in the upstream direction (following the $u-c$ characteristic) and in the downstream direction. The upstream moving waves overtake each other and form a weak shock eventually. A simple qualitative model for this unsteady heat-addition process was given by van Dongen *et al.* (2002). This condensation-induced upstream-moving shock wave can be clearly seen from the pressure histories, as shown in figure 8(*b*), and results in a sharp increase in pressure in the expansion wave. The initial saturation ratio of the mixture is 0.805. Apart from the condensation-induced shock, there is another difference between the dry and wet cases: as a result of latent-heat release to the flow, the pressure level after the passage of the expansion wave is slightly higher in the wet case than in the dry case.

Numerical pressure histories for the dry and wet cases are plotted in figure 9. Because the wall friction and heat transfer are not considered in our present numerical method, the pressures at different positions after the expansion wave have the same level in the dry case, i.e. 0.48 bar, which also agrees with the experimental result at position 1. From a comparison between the experimental and numerical results for humid nitrogen (figures 8(*b*) and 9(*b*), it becomes clear that that the effect of wall

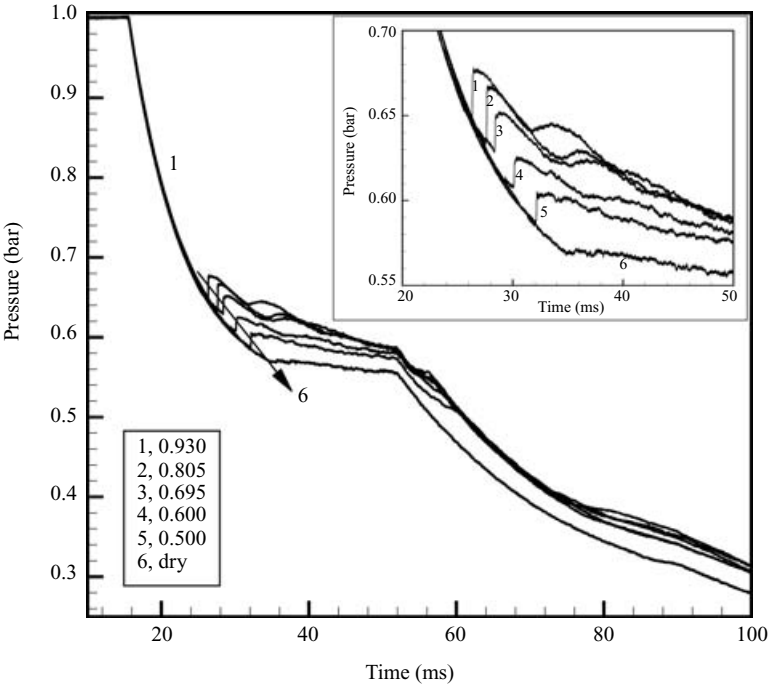

FIGURE 10. Experimental results for pressure histories at position 3 in a Ludwieg tube for different initial saturation ratios.

friction cannot be neglected for the rather large length and time scales considered. The pressure after the weak shock disturbance at position 3 is at the same level in the numerical observation as in the experimental observation, although we know from the 'dry' experiments that friction has a considerable contribution.

Still, an interesting observation can be made for which experiment and simulation agree in a qualitative sense, namely that the weak shock disturbance in trace 3 (figure 8) is followed by a second bump-like pressure disturbance. We shall argue that this is an essential part of the gradual transformation of the 'frozen' initial solution to the asymptotic 'equilibrium' solution as time proceeds. First, we discuss the results of a series of experiments for different humidities, shown in figure 10. It is clear that the strength of the second positive pressure disturbance increases with the initial humidity. A similar trend is found in the numerical simulation, shown in figure 11. A sharp condensation-induced weak shock is followed by a second pressure disturbance.

In order to find an explanation for the observed phenomena, we first refer to a numerical analysis of expansion waves with heterogeneous condensation by Smolders, Niessen & van Dongen (1992). They found that the condensation-induced shock gradually becomes part of the main expansion wave, thereby changing its structure. The relative position of the point of onset of nucleation gradually shifts to a higher pressure level until nucleation is fully quenched locally. This means that at this relative position within the wavefront no more droplets are formed. As a consequence, a new locus of nucleation occurs, shifted now in the direction of the tail of the expansion wavefront. Then the phenomenon repeats, the second compression wave may steepen up and form a second shock wave etc. It was shown that this process asymptotically leads to the formation of a split equilibrium-expansion wave, defined by the equilibrium velocity field u_e and the sound speed c_e.

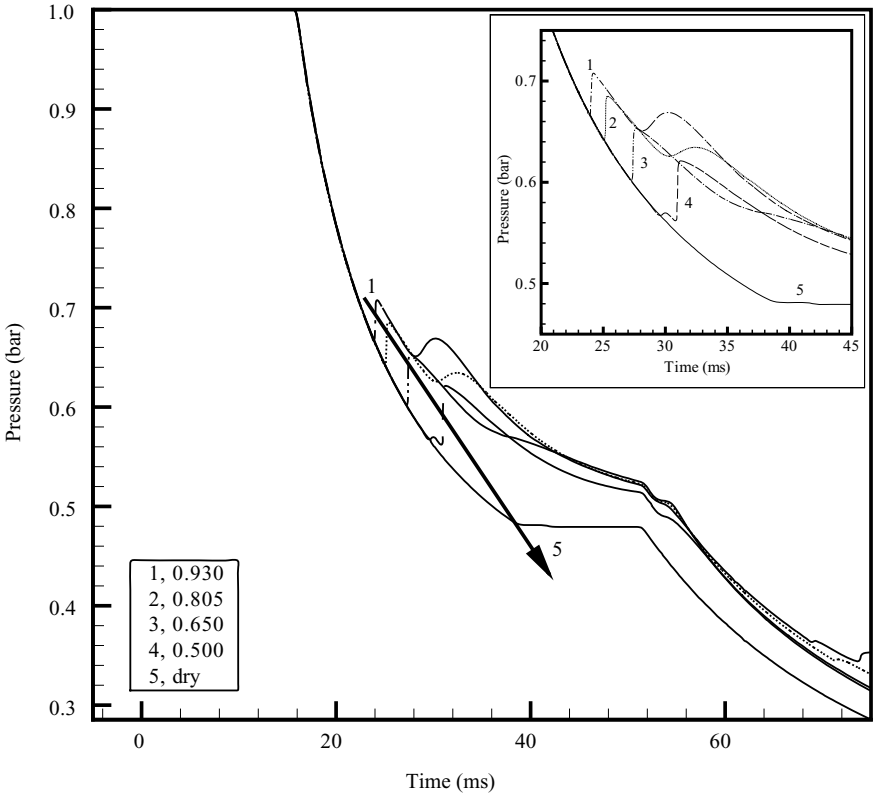

FIGURE 11. Numerical results of pressure histories at position 3 in a Ludwieg tube for different initial saturation ratios.

The equilibrium-expansion wave is again a similarity solution and depends on the similarity coordinate x/t, which equals $u_e - c_e$ for a left-running expansion wave. But the equilibrium sound speed jumps to a lower value, with a jump Δc_e, when passing through vapour–liquid equilibrium from higher to lower temperatures. Since the velocity field is continuous, the consequence is that the expansion fan in equilibrium is split into a 'dry' part and a 'wet' part separated by a plateau of constant conditions, corresponding to phase equilibrium, of extent $\Delta c_e t$. The present numerical simulations and experiments indicate that a similar process takes place with homogeneous nucleation and condensation.

Using the present numerical method, ASCE2D, we studied the development of the condensation phenomena in a rarefaction fan to investigate whether the long-term condensation phenomenon discussed before is also found numerically for homogeneous nucleation. The initial conditions are; $S_{ini} = 0.82$, $T_0 = 298.0\,\mathrm{K}$ the pressure in the high-pressure side (HPS) (on the left side) is 1.0 bar and that in the low-pressure side (LPS) (on the right side) is 0.4 bar. The carrier gas is nitrogen. The results are shown in figure 12 and are plotted as functions of a reduced coordinate, $x/(c_0 t)$, for three different times, 10, 37 and 88 ms.

From the pressure profiles shown in figure 12(*a*), we observe that there is a condensation-induced upstream-moving compression wave (see profile 1), which steepens up and eventually forms a shock wave (see profile 2). As time proceeds the local pressure minimum, which is a balance between the shock wave and the

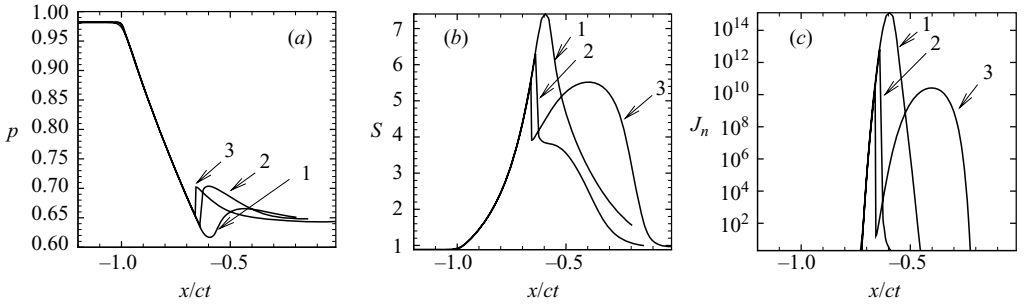

FIGURE 12. Profiles at positions 1, 2 and 3 of (*a*) pressure, (*b*) saturation ratio and (*c*) nucleation rate vs. reduced coordinate at $t = 10$, 37 and 88 ms. The initial conditions are; $S_{ini} = 0.82$, $T_0 = 298.0$ K. The pressure in the HPS (on the left side) is 1.0 bar and that in the LPS (on the right side) is 0.4 bar. The carrier gas is nitrogen.

expansion wave, becomes less deep (see profiles 2 and 3). Therefore the local maximum in the saturation ratio S reduces with time (figure 12*b*). Because the nucleation rate J_n strongly depends on the saturation ratio S, the upstream-moving shock quenches the nucleation process locally. From figure 12(*c*), we can see that at 10 ms the nucleation rate has a very high value in a certain range (1). As time proceeds, the maximum of the nucleation rate decreases and the spatial extent of the nucleation zone becomes smaller (2). At 88 ms, a second nucleation process takes place while the first nucleation becomes even weaker (3). The first nucleation is gradually replaced by the second nucleation at a position further downstream (i.e. to the right). If the tube is sufficient long, a sequence of weaker and weaker compression waves will lead to a plateau in the pressure profile, suggesting an equilibrium condensation process. In that sense, condensation-induced shock formation in an unsteady expansion wave can be interpreted as a first step towards thermodynamic equilibrium. From this point of view, the process is different from the condensation-induced periodic oscillations in slender Laval nozzles, as discussed in the introduction.

5. Condensing flows in the supersonic nozzle G2

The contour profile for nozzle G2 can be found in Lamanna (2000). A typical condensation process in this supersonic nozzle is shown in figure 13. From the axial distribution of the pressure p/p_0, ratio condensate mass fraction g/g_{max} and the nucleation rate J, the details of the condensation process can be obtained. Along the convergent part of the nozzle the pressure decreases, which indicates that the mixture is cooling down. As a consequence, nucleation takes place just upstream of the nozzle throat (at $x = 0$). However, no perturbation of the flow properties is observed. As soon as the droplet-growth process starts a shock appears, owing to the compressive effects from the significant heat release, which quenches the nucleation process locally. As a result, the nucleation rate becomes a sharply peaked function of x. The shock position depends on the humidity. For humidities above a critical value a steady-state shock position is no longer possible and self-sustained oscillations appear, caused by the nonlinear coupling between the flow and the condensation process.

5.1. *Condensation-induced oscillations*

Condensation-induced oscillations in slender Laval nozzles are directly related to the restricted capacity of a flow to absorb heat added to the flow. This capacity

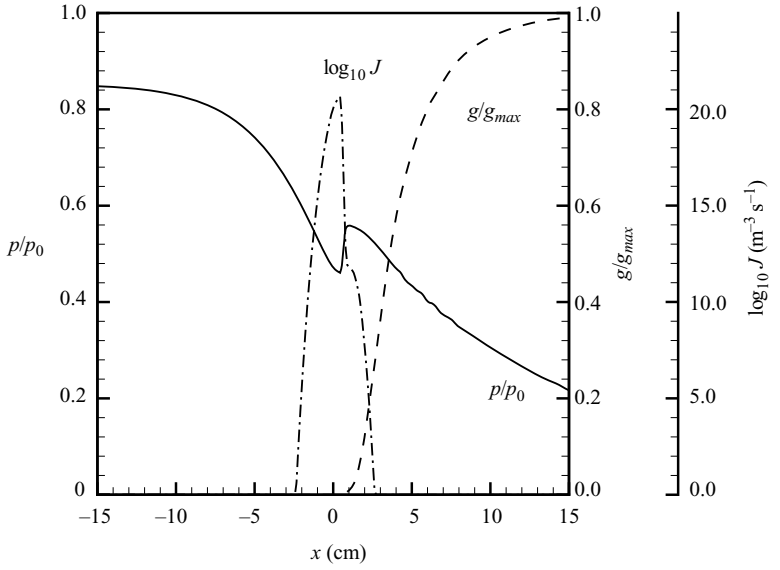

FIGURE 13. Example of a typical condensing flow in the nozzle G2; the axial distribution of pressure p/p_0, condensate mass fraction g/g_{max} and nucleation rate J are shown. The initial conditions are $p_0 = 0.8$ bar, $T_0 = 300.0$ K, $S_{ini} = 0.75$.

depends on the flow Mach number and becomes zero for $M = 1$. If somehow heat is added to such a flow, unsteady pressure waves are generated both in the upstream and downstream directions, which leads to the onset of self-sustained oscillations (Wegener & Cagliostro 1973; Sichel 1981; Frank 1985; Adam & Schnerr 1997; Lamanna 2000). In order to demonstrate condensation-induced oscillations in this nozzle, experiments were done with the following stagnation conditions: $T_o = 282.6$ K, $p_o = 88300$ Pa, $S_o = 1.363$. Two interferograms (preshifted) are shown in figure 14$(c),(d)$ at two different times 0.2 ms apart. The results of the numerical simulation, also in the form of artificial interferometric fringes, are shown in figures 14$(a),(b)$. The vertical solid lines in the numerical interferograms denote the throat position, this is indicated by the left-hand white spots in the experimental interferograms.

Note that each interferogram is the result of a different experiment, since the interferometer is basically designed for the visualization of steady flows. By a careful preparation of the mixture, it is possible to reproduce the stagnation supersaturation within 1 %. The flow proceeds from left to right. At inflow, the density of the mixture is almost constant and thus the fringe pattern stays basically horizontal. Along the nozzle the density decreases and correspondingly the fringe pattern bends downwards. At the condensation shock position the fringe pattern bends upwards, indicating the local increase in the mixture density.

By means of a semi-automatic fringe-counting method, density data are extracted from the interferogram (Lamanna, van Poppel & van Dongen 2002). In figure 15 the experimental density profiles along the nozzle centreline are compared with the numerical results for profiles at different times. The simulations and the experiments show essentially the same trend.

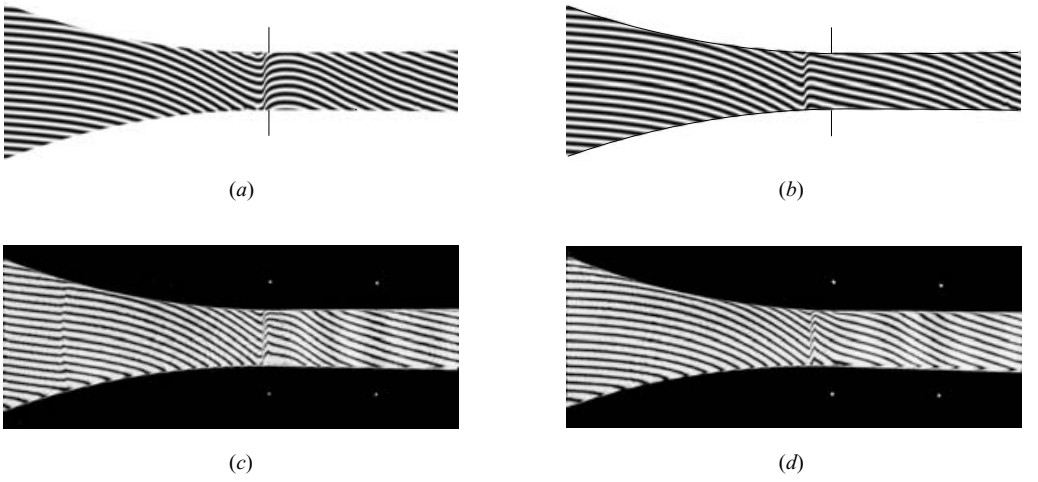

FIGURE 14. Preshifted interferograms obtained in experiments (lower diagrams) and in numerical simulations (upper diagrams) at two different times: (*a*), (*c*) 10.0 ms, (*b*), (*d*) 10.2 ms. Solid lines in the numerical interferograms denote the throat position, which is indicated by the left-hand white spots in the experimental interferograms. The stagnation conditions are: $T_o = 282.6$ K; $p_o = 88\,300$ Pa; $S_o = 1.363$.

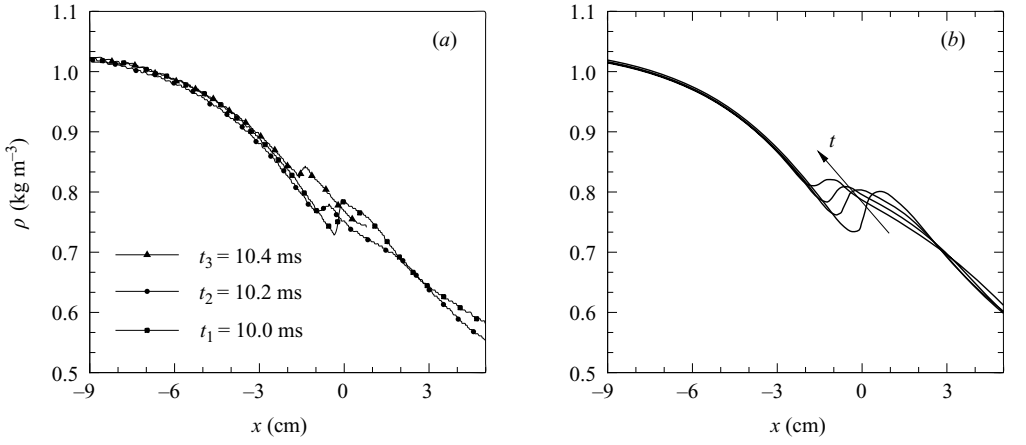

FIGURE 15. (*a*) Experimental and (*b*) numerical density profiles along the nozzle midline. The stagnation conditions are: $T_{tot} = 282.6$ K; $p_{tot} = 88300$ Pa; $S_{tot} = 1.363$. The throat of the nozzle is at $x = 0$.

5.2. *Transition from symmetric to asymmetric oscillation*

Adam & Schnerr (1997) were the first to report the transition from symmetric to asymmetric condensation-induced oscillations in a slender nozzle. It is of interest to see whether different modes of oscillation can be observed in our slender nozzle G2 and whether this is predicted by our numerical model. The oscillations were monitored with a pressure transducer in the nozzle throat. By gradually increasing the initial humidity of the mixture, a situation was found in which the oscillation frequency suddenly increased after some time. Figure 16 (left) shows the detailed experimental pressure signal. Numerically, the transition was not observed within 100 ms for the

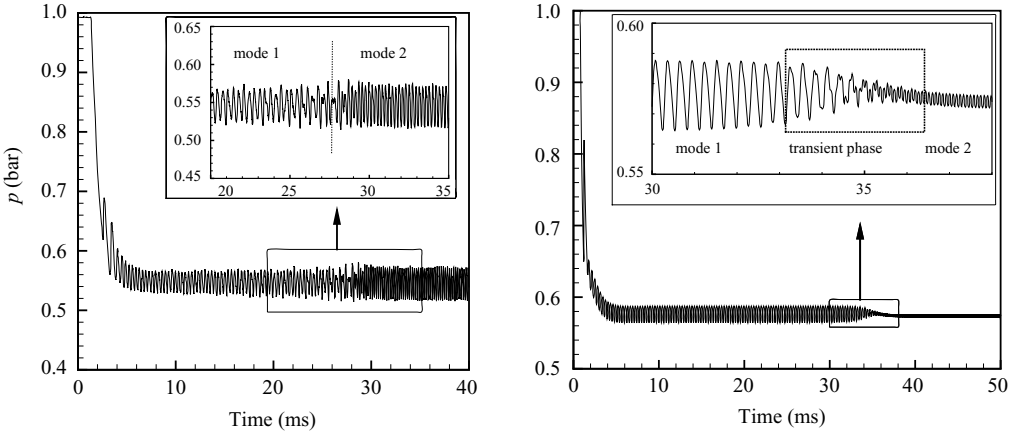

FIGURE 16. Pressure histories at the throat show the transition process of bifurcation in nozzle G2. Left, experimental signal with $S_{ini} = 0.937$; right, numerical simulation with a higher initial supersaturation ($S_{ini} = 1.25$).

same initial saturation ratio as in experiment, i.e. $S_{ini} = 0.937$. Because the higher the initial supersaturation the earlier the transition occurs, the numerical simulation for a higher initial supersaturation ($S_{ini} = 1.25$) shown in figure 16 (right) demonstrates this transition process. Both the experiments and the numerical simulations show first an oscillatory pressure. From the numerical analysis it turns out that the low-frequency mode corresponds to oscillating normal shock waves, while the high-frequency mode corresponds to oscillating oblique shocks. It is found that the amplitude and frequency of the first mode are well described by the simulation. For the second mode, the current numerical method gives a smaller magnitude of the pressure disturbance. However, the pressure disturbance of the second mode has almost the same amplitude as that of the first mode in our experiment. In the numerical results presented by Adam & Schnerr (1997), the amplitude of the pressure disturbance of the second mode is higher than that of the first mode. Furthermore, it should be pointed out that it seems that the moment of transition to a higher frequency in our numerical simulation is always delayed in comparison with the experiment for the same initial condition. This poor prediction of the moment of transition to a higher frequency and of the amplitude of the oscillation indicates that the process is not yet fully understood.

A series of experiments for different initial saturation ratios was carried out. The data given in the literature on frequencies corresponding to mode-1 oscillations were collected by Frank (1985) in a similarity rule that relates frequencies to the cooling rate in the nozzle throat, the maximum liquid mass fraction g_{max} and the initial humidity. He found a proportionality between the reduced frequency $\overline{f}$ and the relative humidity:

$$\overline{f} \equiv \frac{fl}{c^*} a \frac{[(\gamma+1)/2]^{1.5}}{\gamma - 1} g_{max}^{-0.48} = S_{ini}, \tag{5.1}$$

in terms of the nozzle-geometry parameter $l = \sqrt{R^*_{0+} h^*}$, the temperature-gradient parameter

$$a = 0.02663 \left[-\frac{d(T/T_0)}{d(x/h^*)} \right]_*^{0.6012}$$

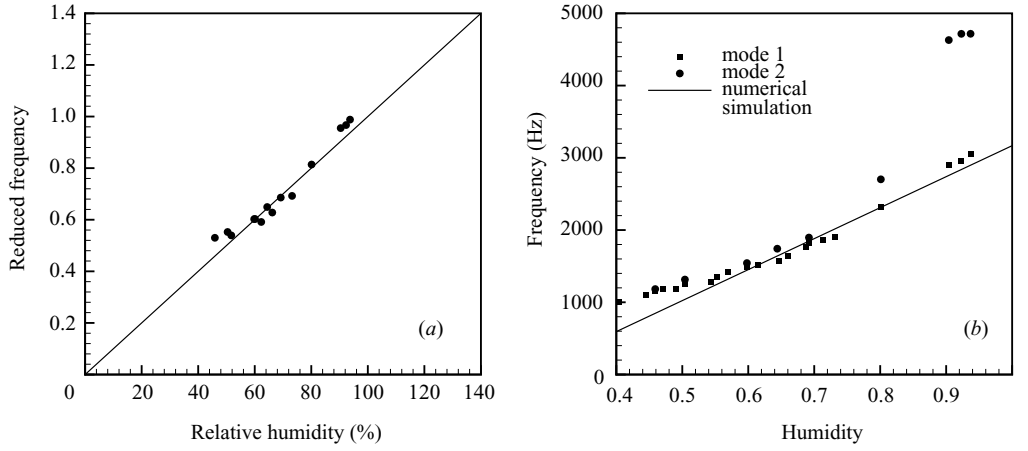

FIGURE 17. (*a*) Dimensionless frequency for the mode-1 oscillation as a function of the relative humidity. The symbols show the experimental data for nozzle G2. The solid line corresponds to the similarity rule of W. Frank (1985). (*b*) Oscillation frequencies of the normal shock mode and of the oblique shock mode as functions of the initial saturation ratio. The symbols show the experimental data. The solid line corresponds to the numerical simulation for the mode-1 oscillation.

and the speed of sound at the nozzle throat, c^*. In figure 17(*a*) the dimensionless frequency of the first mode in our experiments may be compared with the similarity rule of Frank (1985). Our mode-1 data for the G2 nozzle follow the similarity rule. The frequencies for mode-1 and for mode-2 oscillations as functions of the initial humidity are shown in figure 17(*b*). The numerical results for the first mode are also given for comparison. They agree with the experiments and therefore also with the literature data. The experimental threshold humidity for the onset of the oblique shock mode is 70 %. For high initial humidities the experimental value of the mode-2 oscillation tends to a constant value.

6. Vortex shedding and formation of free jets in humid nitrogen

In the third configuration of the Ludwieg tube, as the expansion wave passes the sharp-edged obstacle a starting vortex is produced; this offers the possibility to study the effects of the phase transition on vortex shedding and on the formation of a free jet. The phenomenon is studied by means of the Kistler and Kulite transducers and by means of holographic interferometry, where the fringes directly refer to isodensity contours, and by using schlieren pictures. The experiments were compared with the numerical simulations for both dry and humid nitrogen. Open boundary conditions (i.e. non-reflection boundary conditions) were employed at both the left and the right ends of the computational domain. The interferograms are shown at 'delay' times, defined with respect to the arrival time of the expansion wavefront at the edge of the obstacle. For the numerical isodensity contours the density increment is 0.029 kg m^{-3}.

6.1. *Condensation-induced shock*

After the diaphragm ruptureds, an expansion wave is generated that travels into the tube. As this expansion wave passes the sharp-edged obstacle, a starting vortex is created which develops in time. Figure 18 shows three interferograms with different initial saturation ratio, ($S_{ini} = 0,\ 0.56,\ 0.88$, respectively). If the initial saturation ratio

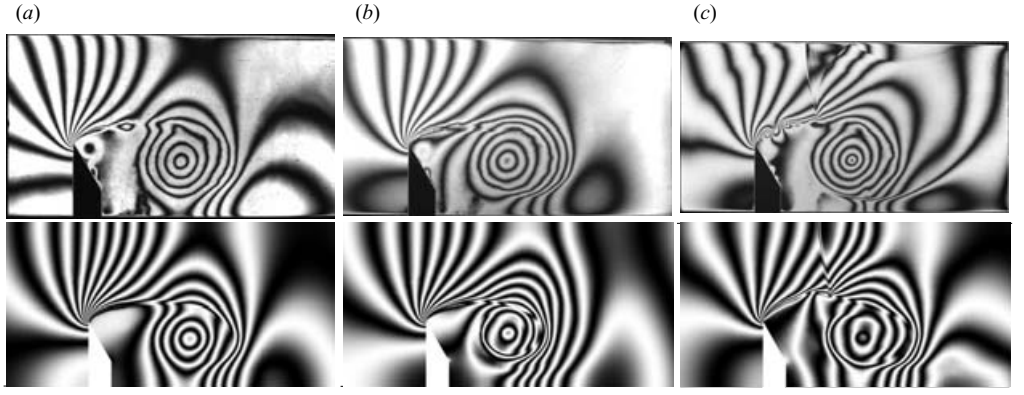

FIGURE 18. Isodensity contours of vortex shedding in a Ludwieg tube for $M_3 = 0.61$ at 1.75 ms. Upper diagrams, the experiments; lower diagrams, the numerical simulations. (*a*) $S_{ini} = 0.0$, (*b*) $S_{ini} = 0.56$, (*c*) $S_{ini} = 0.88$.

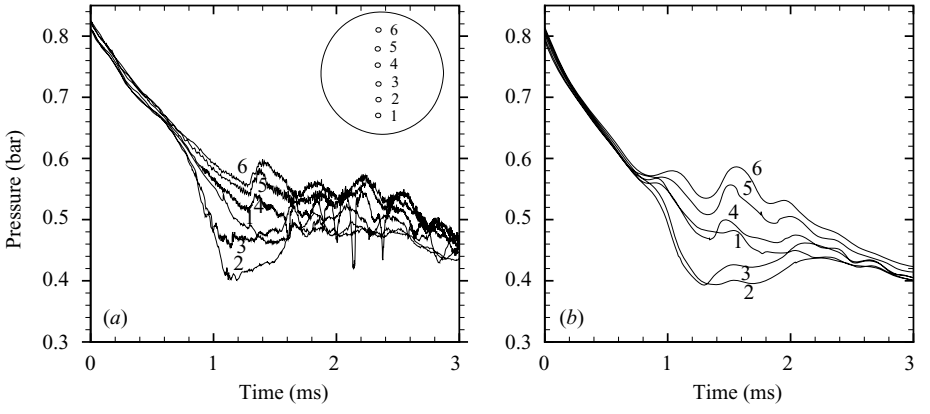

FIGURE 19. Pressure histories from (*a*) Kulite transducers and (*b*) numerical simulation for $M_3 = 0.61$ with $S_{ini} = 0.87$. The legend at upper right in (*a*) shows the position 1–6 across the diameter of the tube.

is sufficiently high, a condensation-induced shock is formed in the one-dimensional unsteady expansion fan, as discussed in § 4. The shock interacts with the starting vortex and the shear layer, generating a very complex flow pattern (figure 18*c*). This represents an interesting example of shock–vortex interaction. The original shock wave, moving from right to left, is fully split by the vortex into two parts, an upper part, clearly visible in figure 18(*c*), which reflects from the transonic shear layer, and a much faster lower part, which is not visible in this figure.

This condensation-induced shock can also be observed in the pressure signals from the Kulite transducer, as shown in figure 19 for $M_3 = 0.61$ and $S_{ini} = 0.87$. A sudden pressure increase present in all the pressure traces is caused by the passage of this shock wave. The condensation-induced shock passage can be seen clearly in traces 4, 5 and 6, but hardly at all in traces 1, 2 and 3. This can be explained by to the interaction of the vortex with the condensation shock.

Transducer 2 gives the lowest pressure value, which implies that, among these six positions, it is the one closest to the trajectory of the vortex core. The pressures near the vortex core in dry and in humid nitrogen are given in figure 20 for a large time

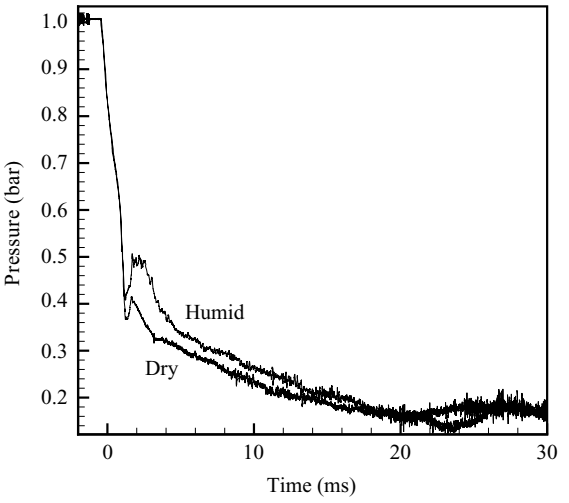

FIGURE 20. The experimental pressure histories for the wet- and dry-nitrogen cases at position 2.

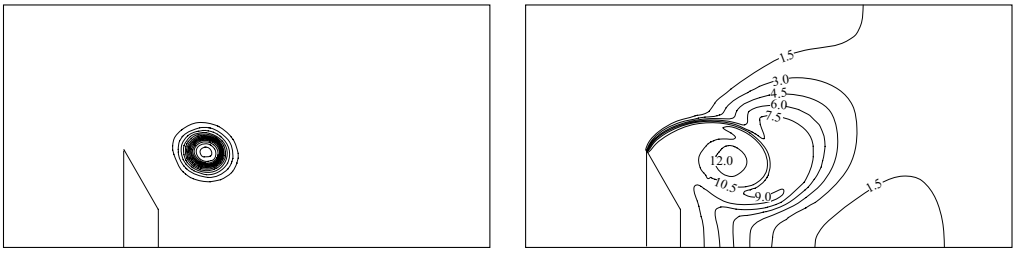

FIGURE 21. Numerical results for the lequid mass fraction g_{H_2O}/kg_N in the Ludwieg tube for $S_{ini} = 0.88$. Left: $M_3 = 0.21$ at 1.4 ms; right: $M_3 = 0.61$ at 1.25 ms.

period. As immediately deducible from the figure, we observe that the local minimum in the pressure due to the expansion and the passage of the vortex in the humid-nitrogen case is higher than that in the dry-nitrogen case, which can be explained as the effect of latent heat released owing to condensation.

6.2. *Condensation in the vortex*

As can be envisaged from figure 18, the numerical isodensity contours do match the experimental isodensity lines reasonably well. However, the secondary vortices are suppressed in the numerical simulation. Furthermore, the vortex deforms more severely in the numerical simulation than in the experiment.

Figure 21 shows the liquid mass fraction in the Ludwieg tube for $M_3 = 0.21$ and for $M_3 = 0.61$. The initial saturation ratio is $S_{ini} = 0.88$. It can be deduced directly that condensation takes place in the vortex core even for a relatively low velocity of the main-stream flow ($M_3 = 0.21$). For this case, the maximum wetness, $g = 0.014$, is located in the vortex core.

In the case of the higher mainstream flow velocity ($M_3 = 0.61$), condensation takes place in both the vortex core and the main flow. Although the maximum wetness ($g = 0.012$) in this figure is still located in the vortex core, the wetness is distributed over a large area. Liquid appears in the main stream, indicating that condensation occurs there as well.

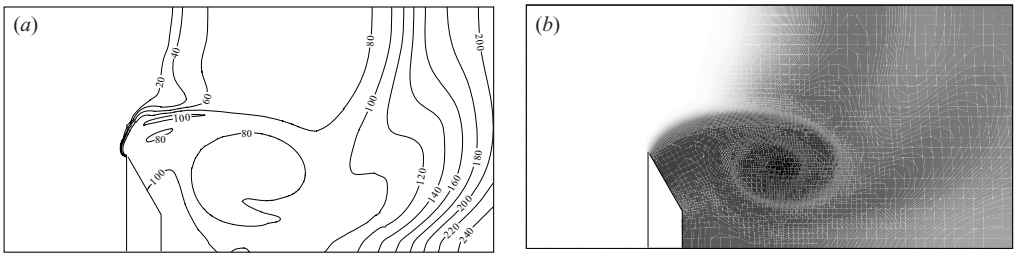

FIGURE 22. Numerical results for (*a*) the modal radius in nm and (*b*) the liquid mass fraction in the Ludwieg tube for $M_3 = 0.61$ and $S_{ini} = 0.88$ at 1.75 ms.

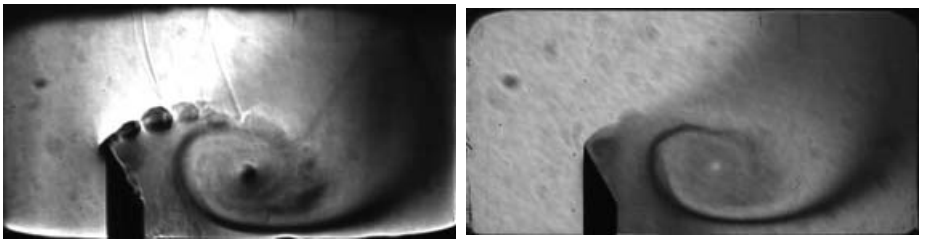

(*a*) (*b*)

FIGURE 23. (*a*) Schlieren and (*b*) light-extinction images of vortex shedding in a Ludwieg tube for $M_3 = 0.61$, $S_{ini} = 0.88$ at 1.25 ms.

As time proceeds, almost all the water vapour in the vortex condenses into liquid. Therefore, a large number of droplets of small size are trapped in the vortex core. Numerical values of modal radius and the wetness distribution at 1.75 ms are shown in figure 22. Note that the modal radius and the liquid mass fraction are almost uniform inside the vortex core ($r = 80$ nm, $g = 0.0135$). A visual interpretation of the wetness distribution in terms of a grey scale is shown in figure 22(*b*) for comparison.

To validate the numerical analysis of wetness in the vortex, schlieren experiments and extinction-field measurements were carried out. The schlieren and extinction-field measurements were done with a similar optical setup. The schlieren 'knife' was formed by a circular orifice in the focal plane of the field lens. The orifice, with diameter 2.0 mm, intercepts the light rays deflected by schlieren effects in the test section. This arrangement is particularly sensitive to density gradients in the radial direction, as expected for vortex flows. If part of the light is scattered by the droplets, the 'schlieren' photograph will combine effects both of density gradient and of light scattering. We can easily suppress the first contribution by using a larger orifice with radius 5.0 mm. As an additional precaution, we suppressed the shadow-graph effect by imaging the central plane of the test section on the sensitive plane of the CCD camera. In this way, schlieren deflection is not recorded and the setup becomes sensitive solely to light extinction caused by the droplets.

Figure 23(*a*) shows a typical combined schlieren and light-extinction snapshot at 1.25 ms for $M_3 = 0.61$ with $S_{ini} = 0.88$. The extinction field (figure 23*b*) reflects the wetness distribution; here the lighter areas indicate less liquid and the darker areas indicate more liquid. The wetness distribution agrees qualitatively well with the numerical result of figure 22(*b*). In the vortex core, however, we clearly observe a bright spot which indicates less extinction of light. It is argued in the Appendix that

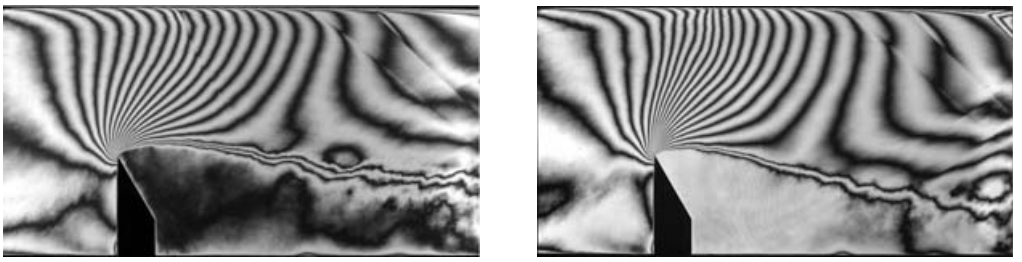

(*a*) (*b*)

FIGURE 24. Experimental isodensity contours taken after a long delay time (15 ms) in a Ludwieg tube for $M_3 = 0.61$. Left, dry nitrogen; right, humid nitrogen with $S_{ini} = 0.92$.

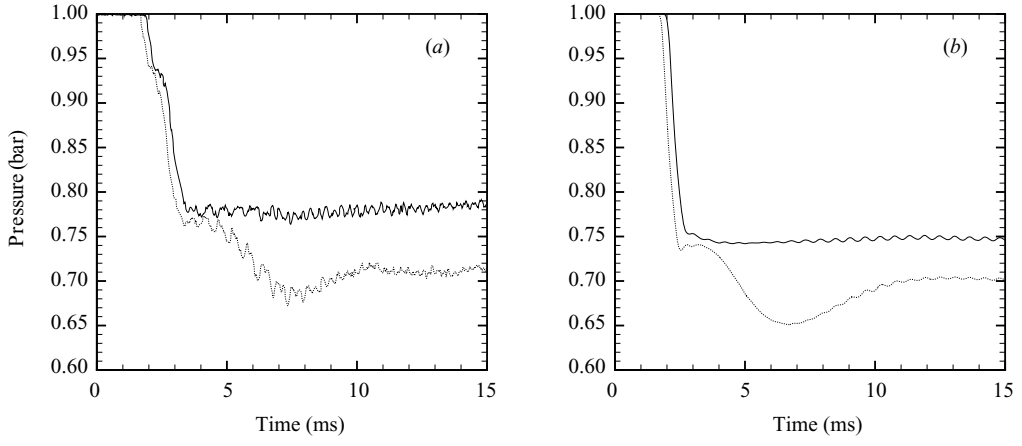

FIGURE 25. Pressure signals from Kistler transducers Pk1 (solid line) and Pk2 (dotted line) for $M_3 = 0.21$, $S_{ini} = 0.88$. (*a*) Experimental result, (*b*) numerical result.

this 'eye' in the mini-hurricane can be explained as an effect of centrifugal drift, not accounted for in the numerical analysis result in figure 22(*b*).

6.3. *Condensation-induced unsteadiness in free jets*

After a certain time, the flow in the mainstream develops into a supersonic jet (figure 24). Because of a small concavity in the top wall (due to inperfections in the stem sealing the hole used to mount pressure transducers), two oblique Mach waves are visible in the main flow. The density fields after a long time delay (15 ms) for $M_3 = 0.61$ both in dry and in humid nitrogen are shown in figure 24. The humid case, with initial saturation ratio 0.92, is only slightly different from the dry-nitrogen case. In the main stream the flow is supersonic, which means that the temperature is very low and condensation is taking place there.

For a relatively high main-flow Mach number $M_3 > 0.2$ and for a relatively high humidity, a condensation-induced oscillation is observed. In figure 25 pressure traces are shown for Kistler transducers Pk1 and Pk2, for $M_3 = 0.21$ and $S_{ini} = 0.88$. It should be noted that Pk1 is located above and slightly downstream of the sharp edge. The pressure traces from both Pk1 and Pk2 show the oscillation. The pressure traces from the numerical simulation give almost the same results as the experiments. The oscillation frequency is about 1.75 kHz with an amplitude of 0.04 bar in the numerical simulation.

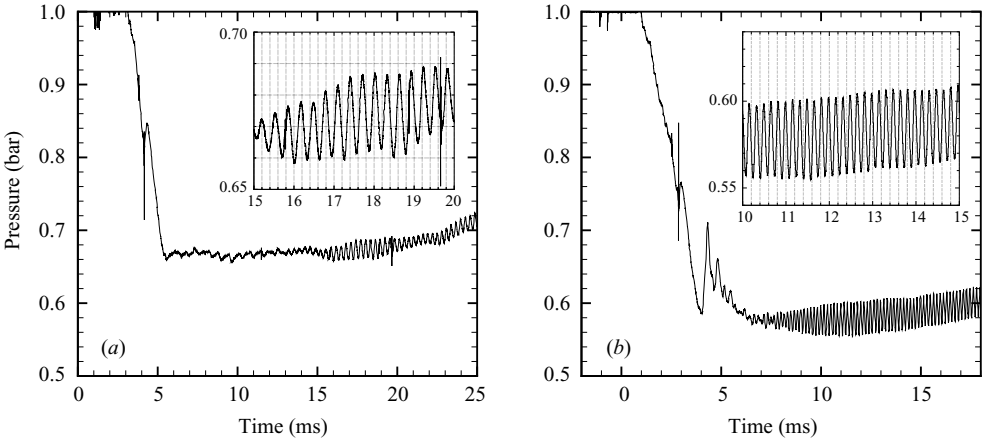

FIGURE 26. Pressure signals from Kistler transducer Pk1 from experiments for (*a*) $M_3 = 0.36$, $S_{ini} = 0.87$, and (*b*) $M_3 = 0.61$, $S_{ini} = 0.88$.

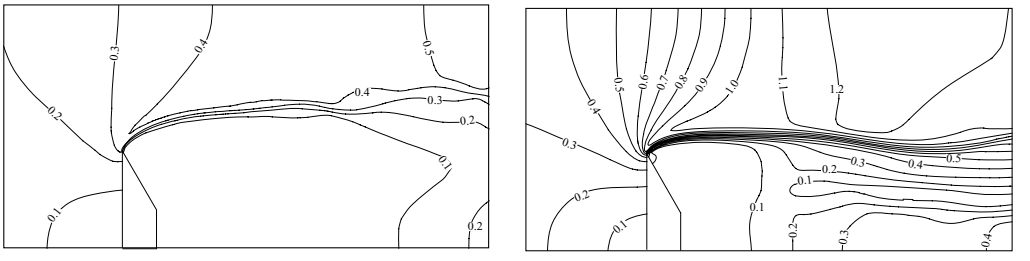

FIGURE 27. Numerical simulation: isoMach lines for $M_3 = 0.21$ (left) and for $M_3 = 0.61$ (right) in a Ludwieg tube with $S_{ini} = 0.88$ at 11.0 ms.

For a higher main-stream velocity, the oscillation is more pronounced. Figure 26 shows the pressure traces of transducer Pk1 for $M_3 = 0.36$ and 0.61, respectively. Transducer Pk1 shows the start of a pressure oscillation at $t = 15$ ms for $M_3 = 0.36$ and somewhat earlier ($t = 8$ ms) for $M_3 = 0.61$. The initial saturation ratio is 0.87 for $M_3 = 0.36$. The oscillation frequency is about 3 kHz. At the higher main-stream velocity ($M_3 = 0.61$, $S_{ini} = 0.88$), a higher frequency (6 kHz) is found. Compared with the experimental result, the oscillation frequency from the numerical simulation (not shown) is much lower, about 2 kHz for $M_3 = 0.61$. The poor agreement with respect to the resonance frequency may have been caused by the limiter (MINMOD) used in our numerical method, which suppresses the high frequencies of oscillations.

As discussed before, condensation-induced oscillations are well known in slender Laval nozzles and in corner expansions for gases with a sufficiently high humidity. To our knowledge, a condensation-induced oscillation for a subsonic free jet separating from a sharp edge has not been observed yet.

In spite of the poor prediction of the resonance frequency, the numerical simulation offers the possibility of studying the mechanism that produces the pressure signal in greater detail. It should be noted that the flow becomes oscillatory after a long time delay, which implies that a free jet with a relatively high velocity has developed. Therefore, the temperature in the main stream is low enough to lead to condensation. Moreover, in the vicinity of the sharp edge the gas has a very low temperature (about 242 K), which leads to high nucleation rates locally. Figure 27 shows contours of

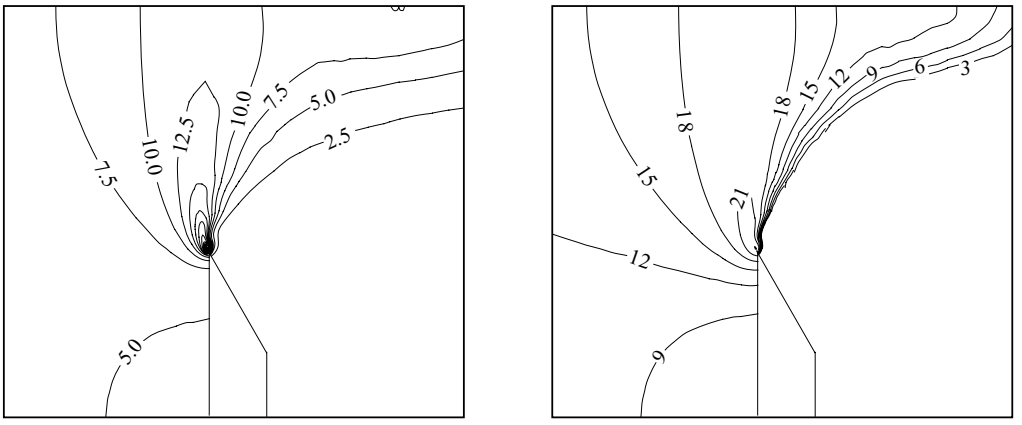

FIGURE 28. Numerical simulation: distributions of the saturation ratio (left) and the nucleation rate (right) in log scale in a Ludwieg tube for $M_3 = 0.61$, $S_{ini} = 0.88$ at 11.0 ms.

Mach numbers at 11.0 ms for $M_3 = 0.21$ and 0.61 with $S_{ini} = 0.88$. For $M_3 = 0.21$, the flow is clearly subsonic in the whole flow field, a situation obviously different from a Prandtl–Meyer expansion. For the case with a high main-stream flow velocity, $M_3 = 0.61$, the flow near the sharp, edge is in the transonic regime.

The corresponding contours of saturation ratio and nucleation rate for $M_3 = 0.61$ are shown in figure 28. Indeed, a very strong nucleation ($J_n \approx 2 \times 10^{24}\,\mathrm{m^{-3}\,s^{-1}}$) occurs in the vicinity of the sharp edge. A large amount of droplets is formed locally, which leads to a rapid growth of the liquid mass fraction. As a consequence, latent heat is added to the flow at a rate which cannot be absorbed by the transonic flow around the edge. As a result pressure waves are generated which modulate nucleation locally. If that occurs, the whole flow field will also be modulated, since waves are generated that propagate in all directions. It seems that the origin of the oscillation is situated near the free shear layer around the sharp edge. As a consequence the structure of the shear layer may have a strong influence on the local nucleation and condensation process, and therefore on the frequency. Because the present numerical method does not resolve well the secondary vortices in the shear layer, as can be seen even for the dry case, the oscillation frequency is not well predicted by the numerical simulation.

7. Summary and conclusions

The effects of homogeneous condensation on compressible flows have been investigated by means of three different types of Ludwieg-tube experiment. Experimental observations have been compared with results from a numerical model, based on a condensation model consisting of a combination of ICCT nucleation theory and the Gyarmathy droplet-growth model. The numerical model, which uses an adaptive unstructured mesh, can handle complex unsteady phenomena in a complex computational domain.

First, the effects of a phase transition on the structure of an unsteady expansion wave in humid nitrogen have been studied, with emphasis on the development of the wave at relatively large length and time scales. Latent heat release has a strong influence on the waveform. The condensation-induced shock which results from latent heat release is gradually absorbed by the expansion-wave, which leads to a persistent deformation of the expansion-wave structure. Then a second shock is formed owing to

a second nucleation process that takes place at a more downstream position. The initial phase of this process, predicted numerically, could also be observed experimentally. It is expected that, for a sufficiently long time, wave splitting will occur, i.e. a plateau in the pressure will be formed separating the dry and wet parts of the expansion wave.

Second, condensation-induced oscillations have been studied in a slender supersonic nozzle G2. Depending on the initial saturation ratio, different flow patterns appear. For sufficiently high initial humidity, condensation-induced oscillations have been found that follow the same similarity rule as in the literature data. Also, good agreement was found between the experimental frequencies and the numerically predicted ones. By further increasing S_{ini}, the oscillation frequency jumps from the basic mode-1 value to a higher value, first reported by Adam & Schnerr (1997) and denoted here as a mode-2 oscillation. From the numerical analysis it follows that a transition from symmetric to asymmetric oscillations takes place. The amplitude and frequency of the mode-2 oscillation are not well predicted by the numerical simulation, and the same holds for the time of onset from mode 1 to mode 2 for the starting nozzle flow.

Third, wave-induced vortex shedding from a sharp edge and the subsequent formation of a free jet have been investigated. Several interesting phenomena due to condensation have been found, as follows.

A condensation-induced shock is formed in the unsteady expansion fan and interacts with the vortex and the shear layer, resulting in a very complex flow field. The pressure and the temperature in the vortex core are slightly higher than in the dry-nitrogen case; this is due to latent-heat release. The secondary vortices are more pronounced than in the dry-nitrogen case. The structure of the 'wet' vortex appears to be slightly different from the 'dry' vortex, which agrees with the numerical simulation.

Condensation is found in the vortex core region as well. An extended wet region is formed after some time, according to the numerical simulation; this is qualitatively confirmed by extinction-field measurements. The extinction-field picture showed that the 'wet' vortex has a relatively 'dry' core, which could be qualitatively explained by centrifugal effects.

At later times, a free jet is formed downstream of the sharp-edged obstacle. Owing to the action of condensation, self-sustained oscillations are found; this is confirmed numerically in a qualitative sense although the frequencies do not yet agree. As a hypothesis, it is suggested that the origin of the oscillation is situated in the free shear layer close to the sharp edge, where the nucleation rate is extremely high. As a consequence the structure of the shear layer may have a strong influence on the local nucleation and condensation process, and therefore on the frequency.

This research was done within the framework of the J. M. Burgerscentrum, Research School for Fluid Mechanics of the Netherlands. Dr Mingyu Sun and Professor K. Takayama provided the source code of VAS2D, which is gratefully acknowledged.

Appendix. Particle drift in a rotating flow field

Consider particles in a rotating flow field with uniform vorticity. The particles have a homogeneous spatial distribution with number density n_d and each has diameter r_d. The quasi-steady-state drift velocity of the particles in a centrifugal force field follows from Stokes law with the Knudsen correction C_k:

$$6\pi\eta r_d V_d C_k = \frac{3\pi}{4}\rho_l r_d^3 \omega^2 r, \tag{A 1}$$

where ρ_l is the density of liquid water, η is the dynamic viscosity of the mixture and ω is the local vorticity. Therefore, the drift velocity of the particles V_d is given by

$$V_d = \frac{2}{9C_k}\frac{r_d^2\rho_l}{\eta}\omega^2 r. \tag{A 2}$$

The particle number density n_d satisfies

$$\frac{\partial n_d}{\partial t} = -\frac{1}{r}\frac{\partial}{\partial r}(r V_d n_d). \tag{A 3}$$

Inserting (A 2) into (A 3) yields

$$\frac{1}{n_d}\frac{\partial n_d}{\partial t} = -\frac{4}{9C_k}\frac{r_d^2\rho_l}{\eta}\omega^2. \tag{A 4}$$

This means that n_d decays uniformly with time constant

$$\tau_d = \frac{9C_k}{4}\frac{\eta}{\rho_l r_d^2\omega^2}. \tag{A 5}$$

The angular velocity ω is related to the circulation Γ according to

$$\omega\pi r_c^2 = \Gamma, \tag{A 6}$$

with r_c the radius of the vortex core.

From the experimental light-extinction picture, we found that $r_c \cong 4\times10^{-3}$ m. From the numerical simulation, we deduced that the vortex circulation $\Gamma \cong 30\,\mathrm{s}^{-1}\,\mathrm{m}^{-1}$. Thus, we can estimate ω:

$$\omega \cong 6\times10^5\mathrm{s}^{-1}. \tag{A 7}$$

For $r_d = 60$ nm and $C_k = 0.6$, we find, for the time constant,

$$\tau_d \cong 10^{-5}\mathrm{s}. \tag{A 8}$$

This means that after 1 ms almost all particles with a diameter of 60 nm would have left the vortex core.

REFERENCES

Abraham, F. F. 1974 *Homogeneous Nucleation Theory*. Academic.

Adam, S. & Schnerr, G. H. 1997 Instabilities and bifurcation of nonequilibrium two-phase flows. *J. Fluid Mech.* **348**, 1–28.

Blythe, P. A. & Shih, C. J. 1976 Condensation shocks in nozzle flows. *J. Fluid Mech.* **76**, 593–621.

Courant, R. & Friedrichs, K. O. 1985 *Supersonic Flow and Shock Waves*, 2nd edn. Springer.

Delale, C. F. & van Dongen, M. E. H. 1998 Thermal choking in two-dimensional expansion flows. *Z. Angew. Math. Phys.* **49**, 515–537.

Delale, C. F., Lamanna, G. & van Dongen, M. E. H. 2001 On stability of stationary shock waves in nozzle flows with homogeneous condensation. *Phys. Fluids* **13**, 2706–2719.

Delale, C. F., Schnerr, G. H. & Zierep, J. 1993*a* Asymptotic solution of transonic nozzle flows with homogeneous condensation. I. Subcritical flows. *Phys. Fluids* A **5**, 2969–2981.

Delale, C. F., Schnerr, G. H. & Zierep, J. 1993*b* Asymptotic solution of transonic nozzle flows with homogeneous condensation. II. Supercritical flows. *Phys. Fluids* A **5**, 2982–2995.

Delale, C. F., Schnerr, G. H. & Zierep, J. 1993*c* The mathematical theory of thermal choking in nozzle flows. *Z. Angew. Math. Phys.* **44**, 943–976.

van Dongen, M. E. H., Luo, X., Lamanna, G. & van Kaathoven, D. J. 2002 On condensation induced shock waves. In *Proc. 10th Chinese Symp. an Shock Waves*, pp. 1–11. Chinese Academy of Science, Yellow Mountain, China.

Frank, W. 1985 Condensation phenomena in supersonic nozzles. *Acta Mechanica* **54**, 135–156.

Gyarmathy, G. 1982 The spherical droplet in gaseous carrier streams: review and synthesis. In *Multiphase Science and Technology*, vol. 1. Springer.

Heath, C. H., Streletzky, K. A., Wyslouzil, B. E., Wölk, J. & Strey, R. 2003 Small angle neutron scattering from $D_2O - H_2O$ nanodroplets and binary nucleation rates in a supersonic nozzle. *J. Chem. Phys.* **118**, 5465–5473.

Hill, P. G. 1966 Condensation of water vapor during supersonic expansion in nozzles. *J. Fluid Mech.* **25**, 593–620.

Holten, V., Labetski, D. G. & van Dongen, M. E. H. 2005 Homogeneous nucleation of water between 200 and 240 K: new wave tube data and estamation of the tolman length. *J. Chem. Phys.* **123**, 104505.

Kashchiev, D. 2000 *Nucleation: Basic Theory with Applications.* Butterworth-Heineman.

Koop, T. 2004 Homogeneous ice nucleation in water and aqueous solutions. *Z. Phys. Chem.* **218**, 1231–1258.

Kotake, S. & Glass, I. I. 1978 Survey of flows with nucleation and condensation. UTIAS Rev. 42. University of Toronto.

Lamanna, G. 2000 On nucleation and droplet growth in condensing nozzle flows. PhD thesis, Eindhoven University of Technology.

Lamanna, G., van Poppel, J. & van Dongen, M. E. H. 2002 Experimental determination of droplet size and density field in condensing flows. *Exps. Fluids* **32**, 381–395.

Lee, J. C. & Rusak, Z. 2001*a* Parametric investigation of nonadiabatic flow around airfoils. *Phys. Fluids* **13**, 315–323.

Lee, J. C. & Rusak, Z. 2001*b* Transonic flow of moist air around a thin airfoil with equilibrium condensation. *J. Aircraft* **38**, 693–720.

Looijmans, K. N. H. & van Dongen, M. E. H. 1997 A pulse-expansion wave tube for nucleation studies at high pressures. *Exps. Fluids* **23**, 54–63.

Ludwieg, H. 1955 Der Rohrwindkanal. *Z. Flugwiss* **3** (7), 206–216.

Ludwieg, H. 1957 Agard report 143. *Tech. Rep.* NATO Headquarters, Scheveningen, Holland.

Luijten, C. C. M. 1998 Nucleation and droplet growth at high pressure. PhD thesis, Eindhoven University of Technology, Eindhoven, The Netherlands.

Luijten, C. C. M., Peeters, P. & van Dongen, M. E. H. 1999 Nucleation at high pressure. II: wave tube data and analysis. *J. Chem. Phys.* **111**, 8535–8544.

Luo, X. 2004 Unsteady flows with phase transition. PhD thesis, Eindhoven University of Technology, Eindhoven, The Netherlands.

Luo, X., Prast, B., van Dongen, M. E. H., Hoeijmakers, H. W. M. & Yang, J. 2006 On phase transition in compressible flows: Modelling and validation. *J. Fuild Mech.* **548**, 403–430.

Mundinger, G. 1994 Numerische Simulation Instationärer Lavaldüsenströmungen mit Energiezufuhr durch Homogene Kondensation. PhD thesis, Universität Karlsruhe, Germany.

Oran, E. S. & Boris, J. P. 1987 *Numerical Simulation of Reactive Flow.* Elsevier.

Oswatitsch, K. 1942 Kondensationserscheinungen in überschalldüsen. *Z. Angew. Math. Mech.* **22**, 1–14.

Owczarek, J. A. 1964 *Fundamentals of Gas Dynamics.* International Co.

Peeters, P., Luijten, C. C. M. & van Dongen, M. E. H. 2001*b* Transitional droplet growth and diffusion coefficients. *Intl J. heat Mass Transfer* **44**, 181–193.

Peeters, P., Pieterse, G. & van Dongen, M. E. H. 2004 Multi-component droplet growth. I. experiments with supersaturated n-nonane vapor and water vapor in methane. *Phys. Fluids* **16**, 2567–2574.

Prandtl 1936 *Atti del Convegno Volta*, 1st edn., vol. XIV. Roma: Reale Academia D'Italia.

Prast, B. 1997 Condensation in supersonic expansion flows: theory and numerical evaluation. SAI, Eindhoven University of Technology, Eindhoven.

Put, F. 2003 Numerical simulation of condensation in transonic flows. PhD thesis, University of Twente, Enschede, The Netherlands.

Put, F., Kelleners, P. H., Hagmeijer, R. & Hoeijmakers, H. W. M. 2001 Numerical simulation of condensing real gas flows. In *Proc. CFD2001.* Atlanta, Ge, USA: ASME PVP-VOL. 424-1.

Rusak, Z. & Lee, J. C. 2000 Transonic flow of moist air around a thin airfoil with nonequilibrium and homogeneous condensation. *J. Fluid Mech.* **403**, 173–199.

Saltanov, G. A. & Tkalenko, R. A. 1975 Investigation of transonic unsteady state flow in the presence of phase transformations. *Zh. Prikl. Mek. ITek. Fiz. (UdSSR)* **6**, 28–42.

Schnerr, G. H., Adam, S. & Mundinger, G. 1994 New modes of perodic shock formation in compressible two-phase flows. In *IUTAM Symp. on Waves in Liquid/Gas and Liquid/Vapor Two-Phase Systems* (ed. S. Morioka & L. van Wijngaarden), pp. 377–386. Kluwer.

Schnerr, G. H. & Dohrmann, U. 1990 Transonic flow around airfoils with relaxation and energy supply by homogeneous condensation. *AIAA J.* **28**, 1187–1193.

Schnerr, G. H. & Dohrmann, U. 1994 Drag and lift in non-adiabatic transonic flow. *AIAA J.* **32**, 101–107.

Sichel, M. 1981 Unsteady transonic nozzle flow with heat addition. *AIAA J.* **19**, 165–177.

Smolders, H. J., Niessen, E. M. J. & van Dongen, M. E. H. 1992 The random choice method applied to non-linear wave propagation in gas-vapour-drolets mixtures. *Computers Fluids* **21** (1), 63–75.

Sun, M. 1998 Numerical and experimental studies of shock wave interaction with bodies. PhD thesis, Tohoku University, Sendai, Japan.

Sun, M. & Takayama, K. 1999 Conservative smoothing on an adaptive quadrilateral grid. *J. Comp. Phys.* **150**, 143–180.

Vargaftik, N. B. 1975 *Tables on the thermophysical properties of liquids and gases*, 2nd edn. Wiley.

Wegener, P. P. 1969 Gasdynamics of expansion flows with condensation and homogeneous nucleation of water vapor. In *Nonequilibrium Flows*, pp. 163–243. Marcel Dekker.

Wegener, P. P. 1975 Nonequilibrium flow with condensation. *Acta Mechanica* **21**, 65–91.

Wegener, P. P. & Cagliostro, D. J. 1973 Periodic nozzle flow with heat addition. *Combust. Sci. Tech.* **6**, 269–277.

Wegener, P. P. & Mack, L. M. 1958 Condensation in supersonic and hypersonic wind tunnels. In *Advances in Applied Mechanics*, vol. 5, pp. 307–447. Academic.

Wegener, P. P. & Mirabel, P. 1987 Homogeneous nucleation in supersaturated vapors. *Natur Wissenschaften* **74**, 111–119.

Wegener, P. P. & Wu, B. J. C. 1977 Gasdynamics and homogeneous nucleation. *Adv. Colloid Interface Sci.* **7**, 326–417.

White, A. J. & Young, J. B. 1993 Time-marching method for prediciton of two-dimensional unsteady flows of condensing steam. *J. Propulsion Power* **9**, 579–587.

Wölk, J. & Strey, R. 2001 Homogeneous nucleation of H_2O and D_2O in comparison: The isotope effect. *J. Phys. Chem.* B **105**, 11683–11701.

Wölk, J., Strey, R., Heath, C. H. & Wyslouzil, B. E. 2002 Empirical function for homogeneous water nucleation rates. *J. Chem. Phys.* **117** (10), 4954–4960.

Zierep, J. 1990 *Strömungen mit Energiezufuhr*, 2nd edn. Karlsruhe: G. Braun.